PHOTONICS Research

Flexible, self-powered, and polarization-sensitive photodetector based on perovskite lateral heterojunction microwire arrays

Shun-Xin Li,[1,2] Jia-Cheng Feng,[1] Yang An,[1] and Hong Xia[1,*]

[1]State Key Laboratory of Integrated Optoelectronics, College of Electronic Science and Engineering, Jilin University, Changchun 130012, China
[2]College of Physics, Jilin University, Changchun 130012, China
*Corresponding author: hxia@jlu.edu.cn

Received 31 May 2023; revised 27 September 2023; accepted 5 October 2023; posted 6 October 2023 (Doc. ID 496838); published 1 December 2023

The fabrication of different perovskite materials with superior properties into lateral heterostructures can greatly improve device performance and polarization sensitivity. However, the sensitivity of perovskites to solvents and environmental factors makes the fabrication of lateral heterojunctions difficult. Here, we realize high-quality perovskite microwire crystal heterojunction arrays using regioselective ion exchange. Photodetectors with responsivity and detectivity up to 748 A W^{-1} and 8.2×10^{12} Jones are fabricated. The photodetector exhibits responsivity as high as 13.5 A W^{-1} at 0 V bias. In addition, the device exhibits ultra-high polarization sensitivity with a dichroic ratio of 5.6, and 81% of its performance was maintained after 144 days of exposure to air.

https://doi.org/10.1364/PRJ.496838

1. INTRODUCTION

As an important component of integrated optoelectronics, the application of photodetectors has expanded from traditional sensing, communication, and imaging to new emerging fields such as flexible robotics and artificial intelligence [1–6]. The expanding application scenarios have more requirements on photodetectors such as low cost, high performance, and flexibility [7–13]. In particular, the self-powered capability of photodetectors and their sensitivity to other information such as polarization are particularly important for some new application scenarios [14,15]. However, photodetectors based on single-component active layers can hardly meet all these requirements at the same time [16–18]. In contrast, careful construction of materials with different optoelectronic properties into heterostructures is a very effective means to achieve photodetectors with multiple advantages [2,19–21].

Compared to vertical heterojunctions, planar lateral heterostructures avoid light loss at multilayer interfaces and have the advantage of easy integration [22]. However, many emerging optoelectronic materials, such as organic–inorganic hybrid perovskites, are difficult to be prepared as lateral heterojunctions due to complex preparation processes [2]. Although heterostructures of organic–inorganic hybrid perovskites and other materials have achieved a variety of high-performance photodetectors and are widely used in imaging, detection, and sensing applications [23–25], it is still challenging to perfectly "stitch" two organic–inorganic hybrid perovskites into a lateral heterostructure [26,27]. The preparation of lateral heterojunctions for conventional inorganic semiconductors is difficult to be directly applied to solvent- and environment-sensitive organic–inorganic hybrid perovskites [2]. For example, Zhao *et al.* realized the preparation of high-quality transverse heterostructures by using ion exchange instead of the traditional solution spin coating method [20]. Moreover, in the process of preparing lateral heterojunctions by the solution method, the material deposited first is easily dissolved by the subsequent solvent [28]. In addition, the large number of grain boundaries and defects in perovskite films not only degrades the performance of the device, but also degrades the device stability [29]. Therefore, it is very important to develop a lateral heterojunction fabrication method suitable for two organic–inorganic hybrid perovskite materials with high-crystal quality for realizing high-performance and stable photodetectors [20].

Here, we propose a nanoimprint-assisted preparation of perovskite microwire crystals combined with ion exchange to fabricate lateral heterostructures and achieve high-performance photodetectors with high polarization sensitivity and environmental stability. After obtaining high-quality perovskite microwire crystals by nanoimprinting, the preparation of high-quality perovskite–perovskite heterojunctions is simply achieved by anion exchange. Benefiting from the high crystal quality and perfect heterojunction interface, the fabricated photodetectors exhibit high performance and outstanding environmental stability. Under a bias of 5 V, the photodetector showed

responsivity, detectivity, EQE, and LDR as high as 748 A W^{-1}, 8.2×10^{12} Jones, 254,187%, and 121 dB, respectively. The photodetector exhibits responsivity and detectivity up to 13.5 A W^{-1} and 1.1×10^{12} Jones under a self-powered condition. Furthermore, the heterojunction endows the device with a high polarization sensitivity of a high dichroic ratio up to 5.6. The device retains 78% of its original performance after 3000 bending cycles. Device performance retains up to 81% after 144 days in air. These results provide ideas for designing high-performance photodetectors.

2. RESULTS AND DISCUSSION

The quantum well structure of a 2D Ruddlesden–Popper type perovskite (PEA)2$(MA)_{n-1}Pb_nX_{3n+1}$ endows it with unique optoelectronic properties, and the substitution of large cations for smaller radius cations enables better stability. Especially when $n = 1$, the unique 2D layered structure endows it with properties like 2D materials. The long hydrophobic organic chain protects the regular octahedral structure of PbX_6, which greatly improves its stability compared with 3D perovskites. Therefore, in this work, $(PEA)_2PbBr_4$ with $n = 1$ was chosen to fabricate a lateral heterojunction [Fig. 1(a)].

High-quality micro/nano-crystals with ordered orientation and suppressed grain boundaries and defects are important for high-performance optoelectronic devices. Here, highly aligned $(PEA)_2PbBr_4$ microwire crystals were first fabricated to serve as platforms for the construction of heterojunctions. The confinement of the flow direction and location of the perovskite precursor solution by nanoimprinting ensures the quality and order of the crystals. As shown in Figs. 1(b) and 1(c), the non-interfering micro-channel array formed by the PDMS template [Appendix A, Fig. 7(a)] and the substrate restricted the flow direction and position of the precursor solution. After the solvent has gradually evaporated completely, the independent liquid strip arrays are transformed into mutually independent microwire crystal arrays. The as-prepared $(PEA)_2PbBr_4$ microwires are not only highly aligned, but also have a smooth surface, which demonstrates their high crystal quality and is beneficial for carrier separation and transport [Appendix A, Fig. 7(b)]. The high crystal quality and order are further demonstrated by the sharp and clear blue fluorescence in the fluorescence micrographs [Appendix A, Fig. 7(c)]. The PDMS template is in close contact with the glass substrate, forming separate channels, and the flow of the solution is restricted within the micrometer-scale one-dimensional channels instead of flowing in arbitrary directions. Therefore, the obtained crystal morphology is still limited by the template and exhibits a layered structure in the direction perpendicular to the substrate [Appendix A, Fig. 7(d)].

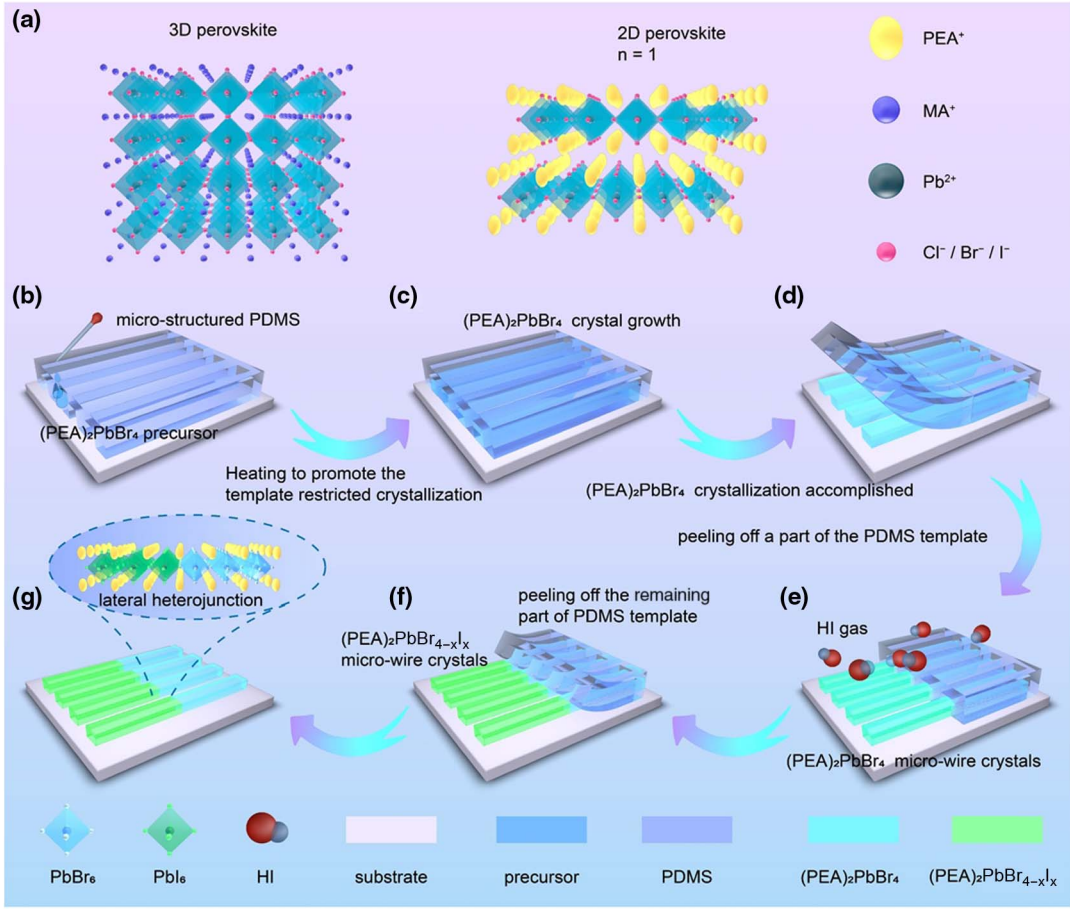

Fig. 1. (a) Schematic diagram of 3D perovskite and 2D Ruddlesden–Popper perovskite structures; (b)–(d) schematic diagram of process for preparing $(PEA)_2PbBr_4$ microwire crystals by imprinting; (e)–(g) regioselective ion exchange preparation of $(PEA)_2PbBr_4$–$(PEA)_2PbBr_{4-x}I_x$ lateral heterojunction.

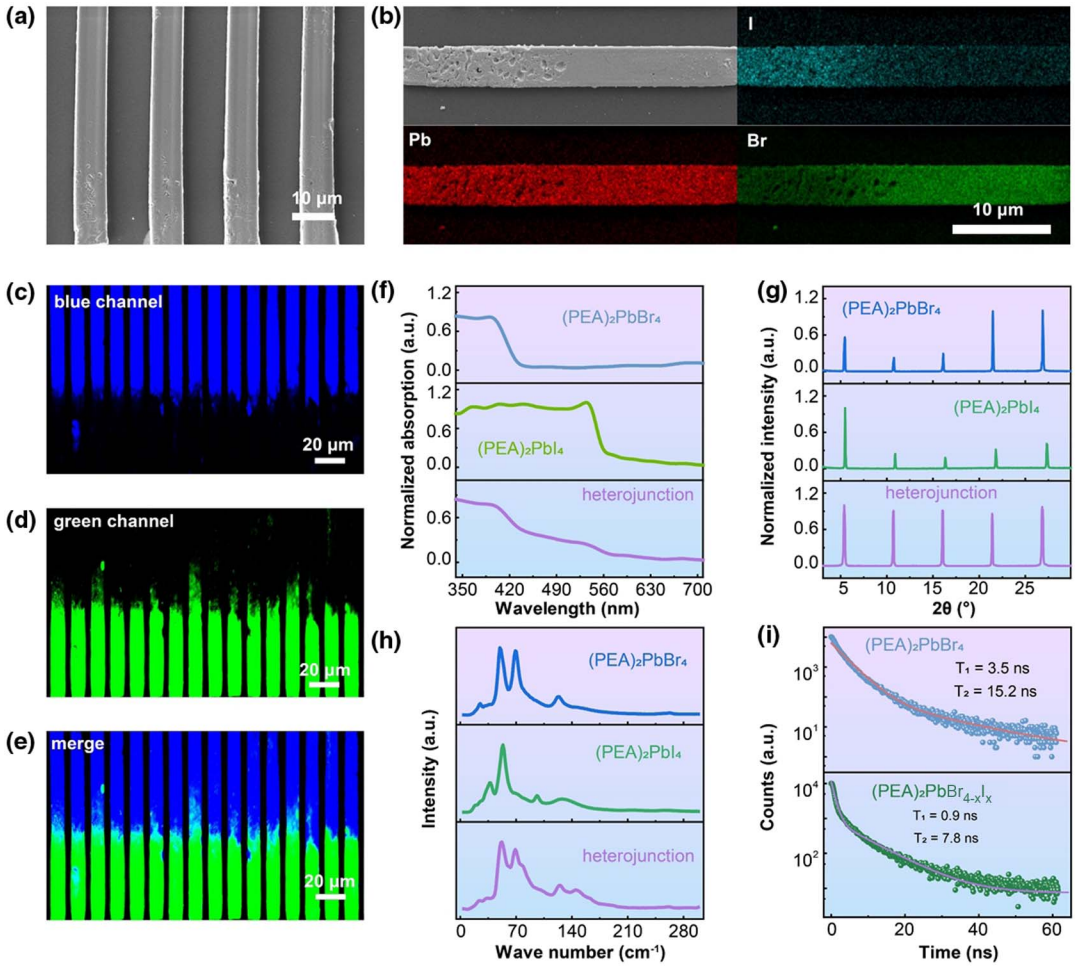

Fig. 2. (a) SEM image of the lateral heterojunction array; (b) I, Pb, Br element distribution of lateral heterojunction; (c)–(e) fluorescence microscope photos of lateral heterojunction array; (f) absorption spectrum, (g) XRD pattern, and (h) Raman spectrum of $(PEA)_2PbBr_{4-x}I_x$, $(PEA)_2PbBr_4$, and $(PEA)_2PbI_4$; (i) typical time-resolved photoluminescence curves of $(PEA)_2PbBr_4$ and $(PEA)_2PbBr_{4-x}I_x$.

The fabrication of high-quality heterojunctions is achieved simply by anion exchange, taking advantage of the reconfigurable anionic bonds of perovskites. To achieve regioselective anion exchange, one half of the PDMS was torn off so that the high-quality microwires were exposed, and the other half was left on the crystal to avoid anion exchange [Fig. 1(d)]. Subsequently, this system was exposed to HI atmosphere [Fig. 1(e)]. With the increase of exposure time, Br in $(PEA)_2PbBr_4$ crystals exposed to HI atmosphere was gradually replaced by I to form $(PEA)_2PbBr_{4-x}I_x$, while the crystals protected by PDMS showed no change in composition. After the anion exchange process was completed, the other half of the PDMS film was peeled off to obtain high-quality and highly ordered $(PEA)_2PbBr_4$–$(PEA)_2PbBr_{4-x}I_x$ lateral heterojunction arrays with clear interfaces [Figs. 1(f) and 1(g)].

The SEM image of the heterojunction shows a clear interface of the $(PEA)_2PbBr_4$–$(PEA)_2PbBr_{4-x}I_x$ lateral heterojunction array [Fig. 2(a)]. The interface and the distribution of elements near the interface were further analyzed by EDS [Fig. 2(b)]. At the end exposed to HI, the Br element in the microwire is greatly reduced, which indicates that a large amount of the Br element is replaced by the I element. At the end protected by PDMS, the distribution of Br elements on the microwires is obviously more than that on the exposed end, indicating that PDMS plays a role in preventing ion exchange for the microwire crystals. Fluorescence microscopy images clearly demonstrated the fluorescence distribution at different positions of the heterojunction [Figs. 2(c)–2(e)]. The bright blue fluorescence in Fig. 2(c) represents the $(PEA)_2PbBr_4$ at the end without ion exchange. The green distribution in Fig. 2(d) represents the $(PEA)_2PbBr_{4-x}I_x$ microwire crystals produced after ion exchange. The two components have a clear boundary, effectively forming a perfectly stitched lateral heterojunction structure [Fig. 2(e)], which is very beneficial for the realization of high-performance devices. The absorption spectrum of Fig. 2(f) shows that the heterojunction possesses both $(PEA)_2PbBr_4$ and $(PEA)_2PbI_4$ absorption peaks. In addition, the XRD pattern shows that $(PEA)_2PbBr_{4-x}I_x$ has the same diffraction pattern as $(PEA)_2PbBr_4$. This indicates that the ion exchange process did not destroy the crystal structure of $(PEA)_2PbBr_4$ microwire crystals [Fig. 2(g)]. Comparing the Raman spectra of $(PEA)_2PbBr_{4-x}I_x$, $(PEA)_2PbBr_4$, and $(PEA)_2PbI_4$, it is found that $(PEA)_2PbBr_{4-x}I_x$ has Raman peaks of both $(PEA)_2PbBr_4$ and $(PEA)_2PbI_4$ [Fig. 2(h)]. Unstable ion gradients can lead

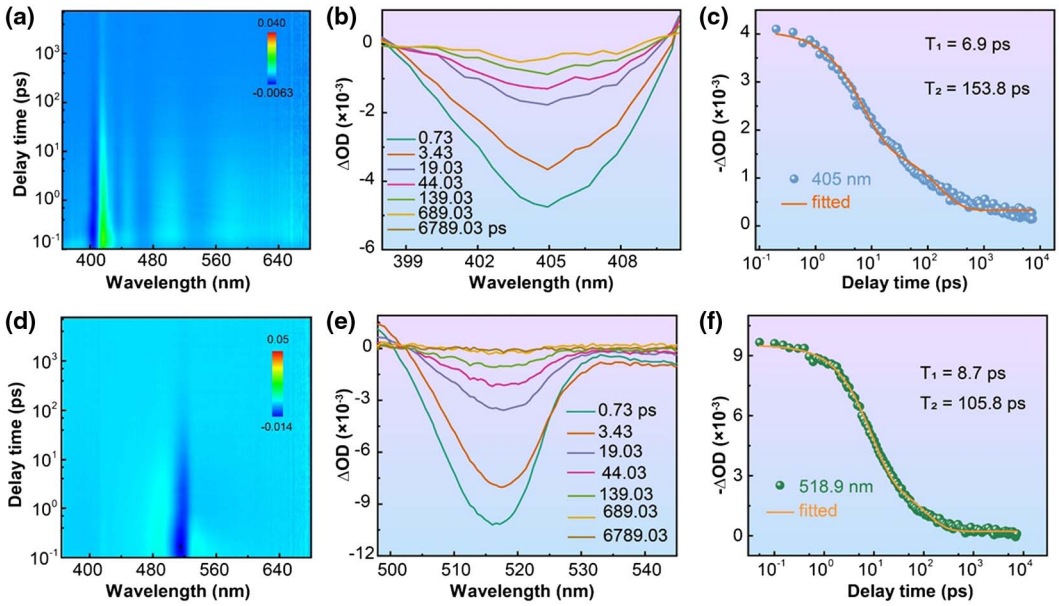

Fig. 3. (a) Color plot of TA spectra from $(PEA)_2PbBr_4$; (b) TA spectra at 398–410 nm; (c) TA kinetics probed at a selected wavelength of 405 nm from (a); (d) color plot of TA spectra from $(PEA)_2PbBr_{4-x}I_x$; (e) TA spectra at 498–545 nm; (f) TA kinetics probed at a selected wavelength of 518.9 nm from (d).

to ion migration, compositional mixing, or structural disorder, thereby reducing the material's stability and shortening its lifespan. Therefore, we have evaluated and characterized the stability of the compositional gradient following the ion exchange process. First, we conducted EDS analysis on the heterojunction stored for 7 days to examine the spatial distribution of elements along the compositional gradient [Appendix B, Figs. 8(a) and 8(b)]. Compared to the initial state, there was no significant change in the element distribution gradient of the heterojunction after 7 days, indicating a slow ion migration process and relative stability of the heterojunction. On the other hand, we characterized the fluorescence distribution of the heterojunction after 7 days of storage. In contrast to EDS analysis, the fluorescent image can more clearly demonstrate ion migration by displaying different colors corresponding to crystal luminescence, thus providing a more intuitive representation of the elemental composition gradient. The fluorescence images showed that the boundary between the blue and green regions of the sample after 7 days was less sharp compared to the initially well-defined fluorescence distribution [Appendix B, Figs. 8(c)–8(e)], indicating a slight change in the compositional gradient due to ion migration.

The time-resolved fluorescence curve is shown in Fig. 2(i). Through double exponential fitting, it is found that the microwire crystal has a nanosecond fluorescence lifetime, suggesting that the heterojunction structure of the micro-wire crystal can well separate the photogenerated carriers and promote the formation of photocurrent. A slight decrease in lifetime after iodide ion exchange has been observed. We speculate that several factors contribute to this phenomenon, including the introduction of water-based HI during the ion exchange process. The decrease in lifetime may be attributed to a combination of factors related to the chemical and physical changes induced by the ion exchange process. Firstly, water content present in the HI solution used for ion exchange can lead to increased moisture absorption by the perovskite crystal. This moisture absorption can cause degradation of the perovskite material, leading to a decrease in carrier lifetime. Furthermore, the ion exchange process itself introduces structural modifications in the perovskite film. During the exchange, iodide ions are substituted with other anions from the HI solution, altering the composition and crystal structure of the perovskite microwires. These changes can result in defects, trap states, and non-radiative recombination sites within the perovskite material, thereby reducing the lifetime of charge carriers and excitons. In addition to these factors, the presence of impurities or contaminants in the HI solution can also contribute to the decreased lifetime. It is essential to ensure the purity and quality of the HI solution to minimize any adverse effects on the perovskite film. Therefore, the decrease in lifetime observed after iodide ion exchange may be a result of multiple factors, including moisture absorption, structural modifications, and impurities introduced during the ion exchange process.

In order to further understand the carrier dynamics in the microwire crystal and the microwire crystal after ion exchange, we have carried out a femtosecond transient absorption test on the microwire crystal before and after ion exchange (Fig. 3), and the excitation wavelength is 365 nm. The TA spectra of these two samples have obvious ground state bleaching peaks. For the sample without ion exchange, the ground state bleaching peak is at 405 nm [Figs. 3(a) and 3(b)]. After ion exchange [Figs. 3(d) and 3(e)], the ground state bleaching peak is located at 518 nm, which is close to the steady-state absorption peak of $(PEA)_2PbI_4$, indicating that after ion exchange, the characteristics of the microwire crystal are closer to $(PEA)_2PbI_4$. The dynamic process of the excited state is also analyzed, as shown in Figs. 3(c) and 3(f). With double exponential fitting, it is

found that both samples have long carrier lifetimes, which is due to the improvement of crystal quality benefitting from the limiting effect of the micron channel on the crystal process. The above results show that the prepared lateral heterostructure is conducive to the separation and transport of carriers, and is very suitable for high-performance optoelectronic devices.

A lateral photoconductive photodetector has been fabricated based on this $(PEA)_2PbBr_4$–$(PEA)_2PbBr_{4-x}I_x$ lateral heterojunction array [Fig. 4(a)]. In this lateral structure, the light is directly irradiated on heterojunctions, avoiding the reflection loss at the interfaces of the multilayer thin film in the vertical structure. Under different bias voltages, the photocurrent I_{photo} of the device increases with the increase of bias voltage. This is because a large bias voltage can separate more photogenerated carriers and thus generate a stronger photocurrent [Fig. 4(b)].

Under 5 V bias, the I_{photo} increases with the enhancement of incident light intensity P_{input}, indicating that more carriers are generated under strong light [Figs. 4(c) and 4(d)]. In the absence of any light, the current I_{dark} of the PD is as low as 0.3 nA [Appendix C, Fig. 9(a)], illustrating that the high crystal quality suppresses defects and grain boundaries. R, an important parameter for evaluating PD performance levels, is calculated up to 748 A W^{-1} ($P_{input} = 7 \times 10^{-6}$ mW/cm^2) according to the following formula:

$$R = \frac{I_{photo} - I_{dark}}{P_{input}}. \tag{1}$$

Two other parameters for evaluating PD performance, detectivity and EQE, are up to 8.2×10^{12} Jones and 254,187%, respectively, according to the following formulas [Appendix C, Fig. 9(b)]:

$$D^* = R\sqrt{\frac{S}{2eI_{dark}}}, \tag{2}$$

$$\mathrm{EQE} = \frac{hcR}{e\lambda} \times 100\%, \tag{3}$$

where S is the device area, h is Planck's constant, c is the speed of light, e is the electron charge, and λ is the wavelength of detected light. LDR, a variation range that characterizes the optical signal detected by the PD without distortion, is calculated according to the following formula:

$$\mathrm{LDR} = 20\log\frac{P_{max}}{P_{min}}, \tag{4}$$

where the P_{max} and P_{min} are the strongest and weakest light intensities that the PD can detect. The LDR of the PD is as high as 121 dB when operating at 5 V bias. The performance of this lateral heterojunction photodetector in the self-powered situation was further explored. As shown in Fig. 4(e), with the enhancement of P_{input}, the I_{Photo} increases significantly, proving that the built-in electric field at the heterojunction can effectively separate many photogenerated carriers without any external bias. At 0 V bias, the dark current of the PD is as low as 7 pA owing to the suppressed carrier trap state [Appendix C, Fig. 9(c)]. Figure 4(f) shows the dependence of I_{photo} and R on light intensity under a self-powered condition. Even without external bias, R is as high as 13.5 A W^{-1}. The D and EQE of the PD are as high as 1.1×10^{12} Jones and 4921%, respectively [Appendix C, Fig. 9(d)]. The above results demonstrate the high crystal quality of the prepared heterojunction, which facilitates the separation and transport of photogenerated carriers. The performance of this lateral heterojunction-based photodetector is outstanding compared to previously reported results (Table 1).

With the continuous expansion of the application scope of PDs, emerging application scenarios have higher and higher requirements for PDs to detect other properties of light, such as polarization information of light. Although the highly anisotropic structures are beneficial to the improvement of the polarization sensitivity of perovskite photodetectors, their

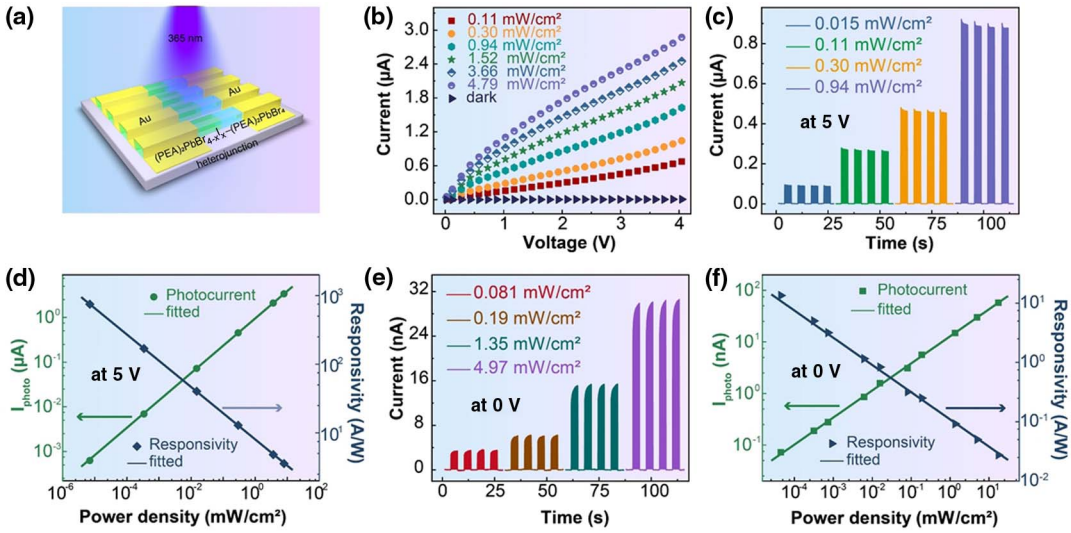

Fig. 4. (a) Sketch of a lateral heterojunction photodetector based on $(PEA)_2PbBr_4$–$(PEA)_2PbBr_{4-x}I_x$; (b) *I-V* curve of PD under different light intensities; (c) *I-t* curve of the PD under different intensities of on–off light irradiation and 5 V bias; (d) variation of photocurrent and R with light intensity under 5 V bias; (e) *I-t* curve of PD under different on–off light intensities and 0 V bias; (f) under 0 V bias, the photocurrent and R versus light intensity.

Table 1. Performance of Perovskite–Perovskite Heterojunction-Based Photodetectors

Materials	λ (nm)	R (A W^{-1})	D (Jones)	Flexible	Long-Term Stability	Reference
BA_2PbI_4–$BA_2MAPb_2I_7$	460	8.12 at 30 V	1.5×10^{12}	No	NA	[1]
$MAPbI_{3-x}Cl_x$–$CsPbBr_3$	405	0.39 at 1 V	5.43×10^{9}	No	NA	[30]
$CsPbI_3$–$CsPbBr_3$	650	0.125 at 0 V	NA	90% after 500 bending cycles	85% after 15 days	[2]
$MAPbI_3$–$MAPbBr_3$	500	<0.2 at 5 V	NA	No	NA	[31]
$iBA_2(MA)_{n-1}Pb_nI_{3n+1}$	405	0.444 at 0 V 3.463 at 1.5 V	4.1×10^{12}	9000 bending cycles	NA	[32]
$(4\text{-AMP})(MA)_2Pb_3Br_{10}$/$MAPbBr_3$	405	1.19×10^{-3} at 0 V	1.26×10^{12}	No	No obvious change after 40 days	[33]
2D/3D perovskite	532	<5 at 2 V	NA	No	71% after 30 days	[34]
$(4\text{-AMP})(MA)_2Pb_3Br_{10}$/$MAPbBr_3$	405	1.5×10^{-3} at 0 V	3.8×10^{10}	No	Negligible degradation after 30 days	[19]
$MAPbBr_3$/$MAPbBr_{3-x}I_x$	532	265 at 5 V	NA	No	90% after 10 days	[20]
$(PEA)_2PbBr_4$ – $(PEA)_2PbBr_{4-x}I_x$	**365**	**748 at 5 V** **13.5 at 0 V**	**8.2×10^{12} at 5 V** **1.1×10^{12} at 0 V**	**78% after 3000 bending cycles**	**81% after 144 days**	**This study**

polarization sensitivity is limited by the isotropic characteristics of the photoelectric properties of perovskite materials. In the heterojunction, the momentum angular distribution of hot carriers excited by linearly polarized light parallel to the heterojunction direction can be mathematically expressed as [19]

$$|\psi|^2 = A^2 + B^2 - 2AB\cos 2\theta. \quad (5)$$

Here, A and B represent the overlap integral between the wave functions of electrons and holes. According to this equation, when subjected to polarization excitation, the momentum of hot carriers is expected to exhibit noticeable directionality. Specifically, when the polarized light aligns with the built-in electric field, the photogenerated carriers acquire maximum momentum along the electric field direction. This efficient carrier

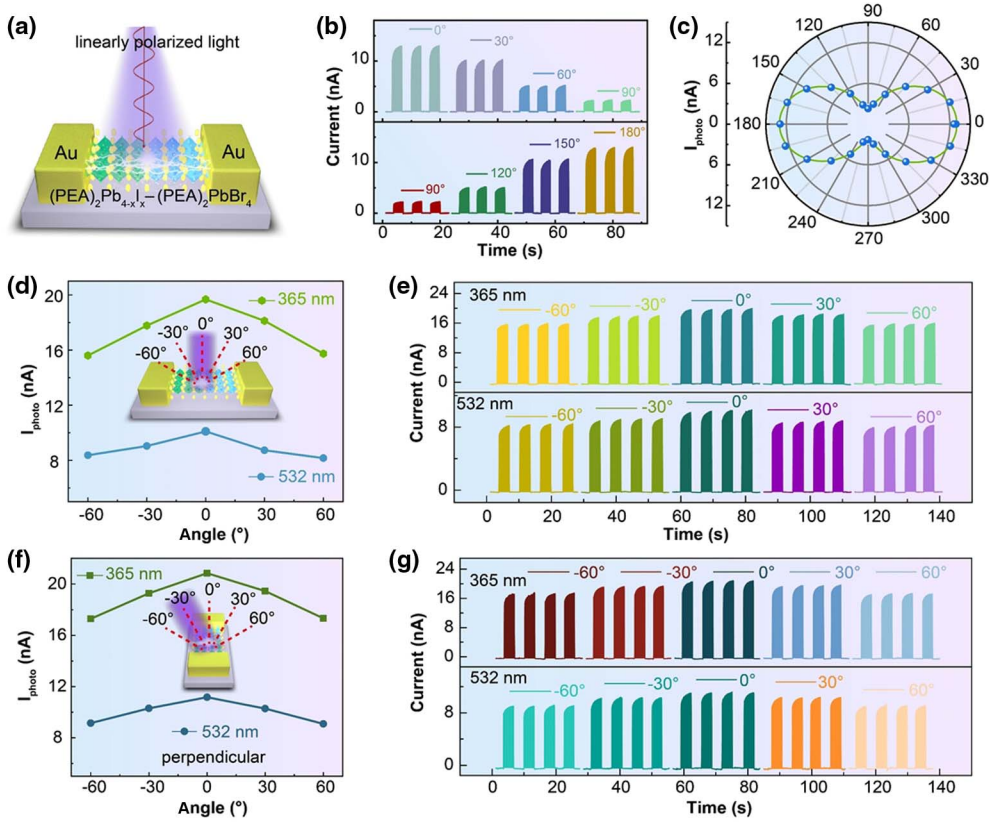

Fig. 5. (a) Sketch of polarized light detection by the lateral heterojunction-based photodetector; (b) *I-t* curve of PD under light irradiation of different polarization angles; (c) photocurrent dependence on the polarization angle of the incident light. When the incident light rotates in the plane of the heterojunction: (d) photocurrent dependence on the angle of the incident light; (e) *I-t* curve of PD under the illumination of different incident angles. When the incident light rotates in the plane perpendicular to the heterojunction: (f) photocurrent dependence on the incident light angle; (g) *I-t* curve of PD under light irradiation at different incident angles.

separation reduces their recombination, resulting in a prominent I_{max}. Conversely, as the polarized light deviates gradually from the built-in electric field direction, the momentum of photogenerated carriers decreases, reaching a minimum when perpendicular to the electric field. Consequently, the separation and transport of excitons become weaker, leading to an ultralow I_{min}. Therefore, the heterojunction structure exhibits significantly enhanced polarization sensitivity compared to single perovskite crystals that rely solely on anisotropic absorption coefficients.

Compared with pure perovskite, the dichroic ratio (I_{max}/I_{min}) of this lateral heterostructure is up to 5.6 [Figs. 5(a)–5(c)]. The polarization sensitivity and device performance of this lateral heterostructure are outstanding compared to previously reported results (Appendix D). The omnidirectional light detection capability of the photodetector is also a very important aspect. Therefore, the response of the PD to different angles of incident light is explored, as shown in Figs. 4(d)–4(g). In the plane parallel to the heterojunction [Figs. 5(d) and 5(e)], the photocurrent decreases gradually with increasing incident angle, but remains at a high level for both UV (365 nm) and green (532 nm) light. When the incident light angle was increased to 60°, the photocurrent remained at 80% (365 nm) and 83% (532 nm) of the original level. Similarly, in the plane perpendicular to the heterojunction [Figs. 5(f) and 5(g)], the I_{photo} decreases with increasing incidence angle, but remains at a very high level. When the incident light angle was increased to 60°, the photocurrent remained at 83% (365 nm) and 82% (532 nm). The above results show that the heterojunction PD has excellent omnidirectional photodetection performance and maintains more than 80% of original photocurrent when the incident angle reaches 60°.

In addition to rigid substrates such as glass, this method is compatible with flexible substrates for the fabrication of flexible PDs. We fabricated a heterojunction-based PD on flexible substrate PET to explore its mechanical flexibility maps [Figs. 6(a)–6(d)]. When the bending angle is as high as 150°, the performance of the device is still up to 74% of the flat state [Figs. 6(a) and 6(b)]. The device durability was also explored, as shown in Figs. 6(c) and 6(d). After 3000 bending cycles, the device retained 78% of its original performance. Due to the sensitivity of organic–inorganic hybrid perovskite to water and oxygen, its poor stability limits the practical application of the device. Benefiting from the protective effect of long hydrophobic organic chains, the prepared heterojunction devices show greatly improved stability. As shown in Figs. 6(e) and 6(f), the I_{photo} of the device remained as high as 86% after exposure in air for up to one month. This is of great significance for organic–inorganic hybrid perovskite-based devices from the laboratory to practical application.

3. CONCLUSION

We demonstrate a method for the fabrication of lateral heterojunctions and realize the fabrication of high-performance

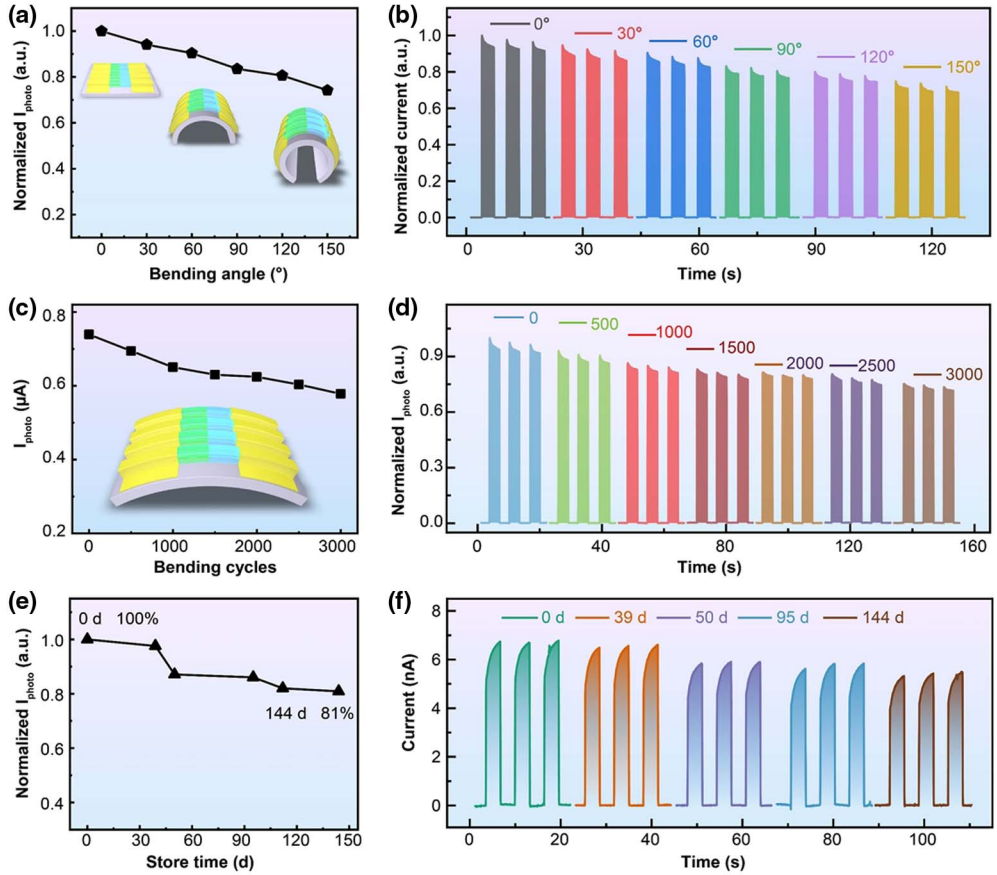

Fig. 6. (a), (b) Photocurrent change curves of PD under different bending states; (c), (d) PD performance after different bending cycles; (e), (f) PD performance after storage in air for different times.

flexible photodetectors with high polarization sensitivity. The fabrication of high-quality 2D Ruddlesden–Popper perovskite microwire crystals was realized by nanoimprinting, and a perfectly stitched lateral heterojunction was realized by a regioselective ion exchange method. Based on this high-quality lateral heterojunction, PDs with *R*, *D*, EQE, and LDR up to 748 A W^{-1}, 8.2×10^{12} Jones, 254,187%, and 121 dB were fabricated. The photodetector exhibits *R* and *D* up to 13.5 A W^{-1} and 1.1×10^{12} Jones under a self-powered condition. This PD not only possesses good mechanical flexibility and omnidirectional light detection capability, but also exhibits polarization sensitivity as high as 5.6. Additionally, it retains 86% of its performance after exposure to air for up to one month. These results provide a new design idea for optoelectronic devices based on perovskite materials from laboratory to practical application.

APPENDIX A: CHARACTERIZATION OF THE MORPHOLOGY OF $(PEA)_2PbBr_4$ MICROWIRE CRYSTALS

Figure 7 shows the SEM image of PDMS template and the basic characterizations of $(PEA)_2PbBr_4$ microwire crystals, including AFM image, fluorescence photo, and cross-sectional SEM image.

APPENDIX B: CHARACTERIZATION OF COMPONENT GRADIENT STABILITY

Figure 8 presents the temporal evolution of the heterojunction composition gradient, including the mapping of I and Br element distribution before and after 7 days, as well as the fluorescence distribution.

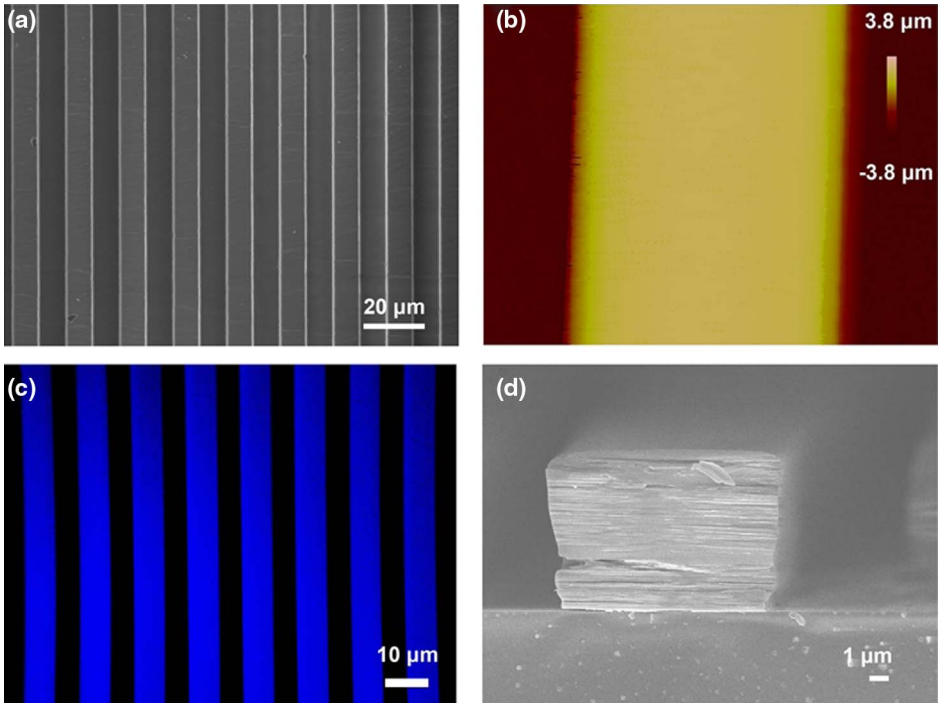

Fig. 7. (a) SEM image of a PDMS template with a microscale striped structure. (b) AFM image of $(PEA)_2PbBr_4$ microwire crystals. (c) Fluorescence microscope photograph of $(PEA)_2PbBr_4$ microwire crystals. (d) SEM image of the cross-section of $(PEA)_2PbBr_4$ microwire crystals.

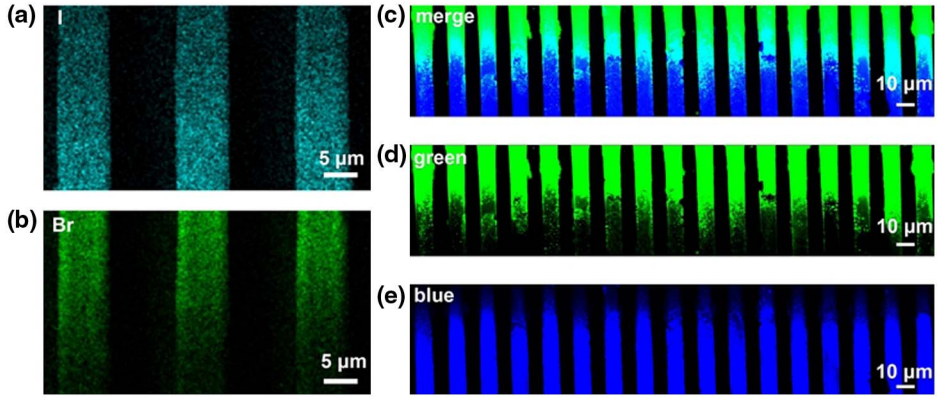

Fig. 8. (a) Mapping of element I after 7 days. (b) Mapping of element Br after 7 days. (c)–(e) Fluorescence microscope images of heterogeneous junctions after 7 days.

APPENDIX C: DARK CURRENT, *D*, AND EQE OF THE PHOTODETECTOR AT 0 V AND 5 V BIAS VOLTAGES

Figure 9 demonstrates the dark current, *D*, and EQE curves of the heterojunction-based photodetector under a bias voltage of 5 V and 0 V.

APPENDIX D: PERFORMANCE OF PEROVSKITE-BASED POLARIZATION-SENSITIVE PHOTODETECTORS

Table 2 provides the performance of perovskite-based polarization-sensitive photodetectors as previously reported.

Funding. National Natural Science Foundation of China (62075081, 21903035, 61825502, 61827826, 61960206003, 62304089); National Key Research and Development Program of China (2020YFA0715000); Natural Science Foundation of Jilin Province (20220101105JC).

Disclosures. The authors declare no conflicts of interest.

Data Availability. All data needed to evaluate the conclusions in the paper are present in the main text and appendices. The datasets generated and analyzed during this study are available from the corresponding author upon reasonable request.

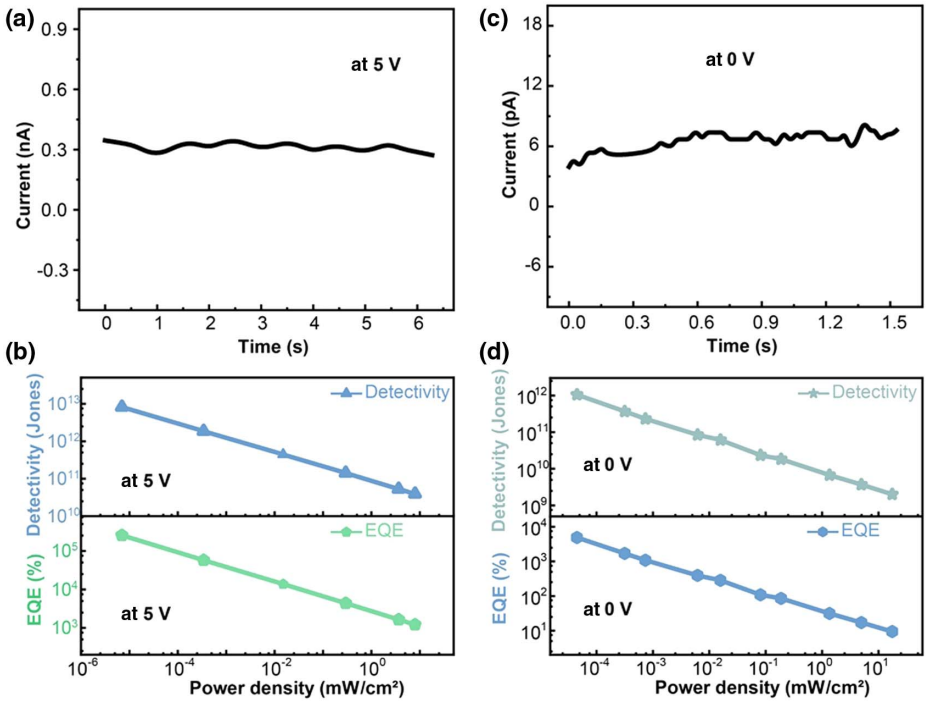

Fig. 9. (a) Dark current of the device at a bias voltage of 5 V. (b) Variation curves of *D* and EQE of the device under different incident light intensities at a bias voltage of 5 V. (c) Dark current of the device at a bias voltage of 0 V. (d) Variation curves of *D* and EQE of the device under different incident light intensities at a bias voltage of 0 V.

Table 2 Performance of Reported Perovskite-Based Polarization-Sensitive Photodetectors

Materials	λ (nm)	Responsivity (A W^{-1})	Anisotropy Ratio	Stability	Reference
$MAPbI_3$	650	15.62 at 5 V	1.58	78.9% after 40 days	[35]
$CsPbBr_3$	513	1377 at 5 V	2.6	NA	[36]
$(iso–BA)_2PbI_4$	560	0.56 at −5 V	1.56	NA	[37]
$(iBA)_2(MA)Pb_2I_7$	637	0.012 at 10 V	1.23	NA	[38]
$(FPEA)_2PbI_4$	520	3.2 at 10 V	2.1	NA	[39]
$MAPbI_3$	530	4.95 at 1 V	0.8–2.6	94% after 30 days	[40]
$(BDA)(EA)_2Pb_3Br_{10}$	405	2.84×10^{-6} at 10 V	4.2–4.8	21 days	[41]
$CsCu_2I_3$	250–350	32.2 at 1 V	3.16	NA	[42]
$(Cl–PMA)_2CsAgBiBr_7$	405	2.4×10^{-4} at 10 V	1.3	NA	[43]
$(AA)_2(EA)_2Pb_3Br_{10}$	405	5×10^{-5} at 0 V	15 at 0 V 1.7 at 10 V	NA	[44]
$(BA)_2(MA)_{n-1}Pb_nBr_{3n+1}$	365	3.5 at 5 V	1.7	81.2% after 5 days	[45]
$CsCu_2I_3/GaN$	325	0.37 at 3 V	28.7	60 days	[46]
$BA_2CsPb_2Br_7$	405	0.0395 at 10 V	1.5	NA	[47]
$(PEA)_2PbBr_4–(PEA)_2PbBr_{4-x}I_x$	**365**	**748 at 5 V, 13.5 at 0 V**	**5.6**	**81% after 144 days**	**This study**

REFERENCES

1. B. Hwang and J. S. Lee, "2D perovskite-based self-aligned lateral heterostructure photodetectors utilizing vapor deposition," Adv. Opt. Mater. **7**, 1801356 (2019).
2. M. Wang, W. Tian, F. R. Cao, M. Wang, and L. Li, "Flexible and self-powered lateral photodetector based on inorganic perovskite $CsPbI_3$-$CsPbBr_3$ heterojunction nanowire array," Adv. Funct. Mater. **30**, 1909771 (2020).
3. B. H. Wang and J. F. Mu, "High-speed Si-Ge avalanche photodiodes," PhotoniX **3**, 22 (2022).
4. Y.-Q. Liu, Z.-D. Chen, D.-D. Han, J.-W. Mao, J.-N. Ma, Y.-L. Zhang, and H.-B. Sun, "Bioinspired soft robots based on the moisture-responsive graphene oxide," Adv. Sci. **8**, 2002464 (2021).
5. Y. S. Guan, J. Qiao, Y. Y. Liang, H. K. Bisoyi, C. Wang, W. Xu, D. B. Zhu, and Q. Li, "A high mobility air-stable n-type organic small molecule semiconductor with high UV-visible-to-NIR photoresponse," Light Sci. Appl. **11**, 236 (2022).
6. Z. Li, T. Yan, and X. Fang, "Low-dimensional wide-bandgap semiconductors for UV photodetectors," Nat. Rev. Mater. **8**, 587–603 (2023).
7. F. Cao, L. Meng, M. Wang, W. Tian, and L. Li, "Gradient energy band driven high-performance self-powered perovskite/CdS photodetector," Adv. Mater. **31**, 1806725 (2019).
8. F. Cao, W. Tian, M. Wang, H. Cao, and L. Li, "Semitransparent, flexible, and self-powered photodetectors based on ferroelectricity-assisted perovskite nanowire arrays," Adv. Funct. Mater. **29**, 1901280 (2019).
9. Y. Gong, X. Xing, Z. Lv, J. Chen, P. Xie, Y. Wang, S. Huang, Y. Zhou, and S.-T. Han, "Ultrasensitive flexible memory phototransistor with detectivity of 1.8×10^{13} Jones for artificial visual nociceptor," Adv. Intel. Syst. **4**, 2100257 (2022).
10. R. C. Lin, Y. M. Zhu, L. Chen, W. Zheng, M. X. Xu, J. L. Ruan, R. F. Li, T. T. Li, Z. G. Lin, L. Cheng, Y. Ding, F. Huang, and X. P. Ouyang, "Ultrafast (600 ps) alpha-ray scintillators," PhotoniX **3**, 9 (2022).
11. N. Wang, W. Yan, Y. Qu, S. Ma, S. Z. Li, and M. Qiu, "Intelligent designs in nanophotonics: from optimization towards inverse creation," PhotoniX **2**, 22 (2021).
12. W. Wang and J. C. Ho, "Luminescent concentrators enable highly efficient and broadband photodetection," Light Sci. Appl. **11**, 125 (2022).
13. Z.-C. Ma, Y.-L. Zhang, B. Han, X.-Y. Hu, C.-H. Li, Q.-D. Chen, and H.-B. Sun, "Femtosecond laser programmed artificial musculoskeletal systems," Nat. Commun. **11**, 4536 (2020).
14. Y. Zhan, Y. Wang, Q. F. Cheng, C. Li, K. X. Li, H. Z. Li, J. S. Peng, B. Lu, Y. Wang, Y. L. Song, L. Jiang, and M. Z. Li, "A butterfly-inspired hierarchical light-trapping structure towards a high-performance polarization-sensitive perovskite photodetector," Angew. Chem. Int. Ed. **58**, 16456–16462 (2019).
15. S.-X. Li, Y. An, X.-C. Sun, H. Zhu, H. Xia, and H.-B. Sun, "Highly aligned organic microwire crystal arrays for high-performance polarization-sensitive photodetectors and image sensors," Sci. China Mater. **65**, 3105–3114 (2022).
16. C. Chen, Y. Yang, X. Zhou, W. Xu, Q. Cui, J. Lu, H. Jing, D. Tian, C. Xu, T. Zhai, and H. Xu, "Synthesis of large-area uniform MoS_2-WS_2 lateral heterojunction nanosheets for photodetectors," ACS Appl. Nano Mater. **4**, 5522–5530 (2021).
17. S.-X. Li, Y.-S. Xu, C.-L. Li, Q. Guo, G. Wang, H. Xia, H.-H. Fang, L. Shen, and H.-B. Sun, "Perovskite single-crystal microwire-array photodetectors with performance stability beyond 1 year," Adv. Mater. **32**, 2001998 (2020).
18. P. S. Wu, L. Ye, L. Tong, P. Wang, Y. Wang, H. L. Wang, H. N. Ge, Z. Wang, Y. Gu, K. Zhang, Y. Y. Yu, M. Peng, F. Wang, M. Huang, P. Zhou, and W. D. Hu, "Van der Waals two-color infrared photodetector," Light Sci. Appl. **11**, 9 (2022).
19. X. Zhang, L. Li, C. Ji, X. Liu, Q. Li, K. Zhang, Y. Peng, M. Hong, and J. Luo, "Rational design of high-quality 2D/3D perovskite heterostructure crystals for record-performance polarization-sensitive photodetection," Natl. Sci. Rev. **8**, nwab044 (2021).
20. Y. W. Guan, C. H. Zhang, Z. Liu, Y. M. Zhao, A. Ren, J. Liang, F. Q. Hu, and Y. S. Zhao, "Single-crystalline perovskite p-n junction nanowire arrays for ultrasensitive photodetection," Adv. Mater. **34**, 2203201 (2022).
21. R. J. Tian, X. T. Gan, C. Li, X. Q. Chen, S. Q. Hu, L. P. Gu, D. Van Thourhout, A. Castellanos-Gomez, Z. P. Sun, and J. L. Zhao, "Chip-integrated van der Waals PN heterojunction photodetector with low dark current and high responsivity," Light Sci. Appl. **11**, 101 (2022).
22. M. Wang, W. Tian, F. Cao, M. Wang, and L. Li, "Flexible and self-powered lateral photodetector based on inorganic perovskite $CsPbI_3$-$CsPbBr_3$ heterojunction nanowire array," Adv. Funct. Mater. **30**, 1909771 (2020).
23. Y. Cao, X. Sha, X. Bai, Y. Shao, Y. Gao, Y.-M. Wei, L. Meng, N. Zhou, J. Liu, B. Li, X.-F. Yu, and J. Li, "Ultralow light-power consuming photonic synapses based on ultrasensitive perovskite/indium-gallium-zinc-oxide heterojunction phototransistors," Adv. Electron. Mater. **8**, 2100902 (2021).
24. L. L. Gu and Z. Y. Fan, "Perovskite/organic-semiconductor heterojunctions for ultrasensitive photodetection," Light Sci. Appl. **6**, e17090 (2017).
25. D. Hao, D. Liu, Y. Shen, Q. Shi, and J. Huang, "Air-stable self-powered photodetectors based on lead-free $CsBi_3I_{10}/SnO_2$ heterojunction for weak light detection," Adv. Funct. Mater. **31**, 2100773 (2021).
26. E. Z. Shi, B. Yuan, S. B. Shiring, Y. Gao, Akriti, Y. F. Guo, C. Su, M. L. Lai, P. D. Yang, J. Kong, B. M. Savoie, Y. Yu, and L. T. Dou, "Two-dimensional halide perovskite lateral epitaxial heterostructures," Nature **580**, 614–620 (2020).
27. S. C. Zhang, Z. Y. Lin, E. Z. Shi, B. P. Finkenauer, Y. Gao, A. J. Pistone, K. Ma, B. M. Savoie, and L. T. Dou, "Quantifying anionic diffusion in 2D halide perovskite lateral heterostructures," Adv. Mater. **33**, 2105183 (2021).
28. S. X. Li, H. Xia, L. Wang, X. C. Sun, Y. An, H. Zhu, B. F. Bai, and H. B. Sun, "Self-powered and flexible photodetector with high polarization sensitivity based on $MAPbBr_3$-$MAPbI_3$ microwire lateral heterojunction," Adv. Funct. Mater. **32**, 2206999 (2022).
29. S. X. Li, H. Xia, X. C. Sun, Y. An, H. Zhu, and H. B. Sun, "Curved photodetectors based on perovskite microwire arrays via *in situ* conformal nanoimprinting," Adv. Funct. Mater. **32**, 2202277 (2022).
30. Y. Yang, H. T. Dai, F. Yang, Y. T. Zhang, D. Luo, X. L. Zhang, K. Wang, X. W. Sun, and J. Q. Yao, "All-perovskite photodetector with fast response," Nanoscale Res. Lett. **14**, 291 (2019).
31. N. T. Shewmon, H. Yu, I. Constantinou, E. Klump, and F. So, "Formation of perovskite heterostructures by ion exchange," ACS Appl. Mater. Interfaces **8**, 33273–33279 (2016).
32. Z. X. Lai, Y. Meng, Q. Zhu, F. Wang, X. M. Bu, F. Z. Li, W. Wang, C. T. Liu, F. Wang, and J. C. Ho, "High-performance flexible self-powered photodetectors utilizing spontaneous electron and hole separation in quasi-2D halide perovskites," Small **17**, 2100442 (2021).
33. X. Y. Zhang, C. M. Ji, X. T. Liu, S. S. Wang, L. N. Li, Y. Peng, Y. P. Yao, M. C. Hong, and J. H. Luo, "Solution-grown large-sized single-crystalline 2D/3D perovskite heterostructure for self-powered photodetection," Adv. Opt. Mater. **8**, 2000311 (2020).
34. C. W. Jang, H. Kim, M. K. Nazeeruddin, D. H. Shin, and S. H. Choi, "Piezo-electric and -phototronic effects of perovskite 2D/3D heterostructures," Nano Energy **84**, 105899 (2021).
35. Q. Song, Y. Wang, F. Vogelbacher, Y. Zhan, D. Zhu, Y. Lan, W. Fang, Z. Zhang, L. Jiang, Y. Song, and M. Li, "Moire perovskite photodetector toward high-sensitive digital polarization imaging," Adv. Energy Mater. **11**, 2100742 (2021).
36. J. Feng, X. Yan, Y. Liu, H. Gao, Y. Wu, B. Su, and L. Jiang, "Crystallographically aligned perovskite structures for high-performance polarization-sensitive photodetectors," Adv. Mater. **29**, 1605993 (2017).
37. L. Li, L. Jin, Y. Zhou, J. Li, J. Ma, S. Wang, W. Li, and D. Li, "Filterless polarization-sensitive 2D perovskite narrowband photodetectors," Adv. Opt. Mater. **7**, 1900988 (2019).
38. Y. Liu, Z. Wu, X. Liu, S. Han, Y. Li, T. Yang, Y. Ma, M. Hong, J. Luo, and Z. Sun, "Intrinsic strong linear dichroism of multilayered 2D hybrid perovskite crystals toward highly polarized-sensitive photodetection," Adv. Opt. Mater. **7**, 1901049 (2019).

39. M. Li, S. Han, B. Teng, Y. Li, Y. Liu, X. Liu, J. Luo, M. Hong, and Z. Sun, "Minute-scale rapid crystallization of a highly dichroic 2D hybrid perovskite crystal toward efficient polarization-sensitive photodetector," Adv. Opt. Mater. **8**, 2000149 (2020).
40. L. Gao, K. Zeng, J. Guo, C. Ge, J. Du, Y. Zhao, C. Chen, H. Deng, Y. He, H. Song, G. Niu, and J. Tang, "Passivated single-crystalline $CH_3NH_3PbI_3$ nanowire photodetector with high detectivity and polarization sensitivity," Nano Lett. **16**, 7446–7454 (2016).
41. H. Ye, Y. Peng, X. Shang, L. Li, Y. Yao, X. Zhang, T. Zhu, X. Liu, X. Chen, and J. Luo, "Self-powered visible-infrared polarization photodetection driven by ferroelectric photovoltaic effect in a Dion–Jacobson hybrid perovskite," Adv. Funct. Mater **32**, 2200223 (2022).
42. Y. Li, Z. Shi, L. Wang, Y. Chen, W. Liang, D. Wu, X. Li, Y. Zhang, C. Shan, and X. Fang, "Solution-processed one-dimensional $CsCu_2I_3$ nanowires for polarization-sensitive and flexible ultraviolet photodetectors," Mater. Horiz. **7**, 1613–1622 (2020).
43. W. Wu, Z. Xu, Y. Yao, Y. Liu, G. Long, L. Li, M. Hong, and J. Luo, "Realization of in-plane polarized light detection based on bulk photovoltaic effect in a polar van der Waals crystal," Small **18**, 2200011 (2022).
44. Y. Peng, X. Liu, Z. Sun, C. Ji, L. Li, Z. Wu, S. Wang, Y. Yao, M. Hong, and J. Luo, "Exploiting the bulk photovoltaic effect in a 2D trilayered hybrid ferroelectric for highly sensitive polarized light detection," Angew. Chem. Int. Edit. **59**, 3933–3937 (2020).
45. S. X. Li, G. P. Zhang, H. Xia, Y. S. Xu, C. Lv, and H. B. Sun, "Template-confined growth of Ruddlesden-Popper perovskite microwire arrays for stable polarized photodetectors," Nanoscale **11**, 18272–18281 (2019).
46. C. Zou, Q. Liu, K. Chen, F. Chen, Z. Zhao, Y. Cao, C. Deng, X. Wang, X. Li, S. Zhan, F. Gao, and S. Li, "A high-performance polarization-sensitive and stable self-powered UV photodetector based on a dendritic crystal lead-free metal-halide $CsCu_2I_3$/GaN heterostructure," Mater. Horiz. **9**, 1479–1488 (2022).
47. J. Wang, Y. Liu, S. Han, Y. Ma, Y. Li, Z. Xu, J. Luo, M. Hong, and Z. Sun, "Ultrasensitive polarized-light photodetectors based on 2D hybrid perovskite ferroelectric crystals with a low detection limit," Sci. Bull. **66**, 158–163 (2021).